Parallel multi-stacked photoanodes of Sb-doped *p−n* homojunction hematite with near-theoretical solar conversion efficiency

Chenyang Xu[1], Hongxin Wang[1], Hongying Guo[1], Ke Liang[1], Yuanming Zhang[1], Weicong Li[1], Junze Chen [1,2] ✉, Jae Sung Lee [3] ✉ & Hemin Zhang [1,2] ✉

Developing transparent and efficient photoanodes is a challenging but essential task in tandem photoelectrochemical cell for unassisted solar water splitting without an external bias. Here we report construction of *p−n* homojunction hematite photoanodes by hybrid microwave annealing-induced single antimony doping, which results in the gradually-increased valence states from the surface to the inside by the unique features of hybrid microwave annealing. The Sb-doped *p−n* homojunction hematite photoanode exhibits improved performance and displays a good transparency, achieving a stable photocurrent density of ~4.21 mA cm^{-2} at 1.23 V$_{RHE}$ under 100 mW cm^{-2} solar irradiation, which is comparable to the reported state-of-the-art hematite photoanodes. More importantly, a parallel-connected stack of six photoanodes of transparent *p−n* homojunction records a near-theoretical photocurrent density of ~10 mA cm^{-2} at 1.23 V$_{RHE}$ under standard photoelectrochemical water splitting conditions, which serves as a useful reference for hematite photoanodes and promises its practical application for unbiased photoelectrochemical water splitting.

Sunlight and water are two of the most abundant natural resources available on earth. Production of 'green' hydrogen by photoelectrochemical (PEC) water splitting offers a promising pathway towards carbon neutrality via supplying a clean, renewable and sustainable fuel[1,2]. Photoelectrodes based on metal oxide semiconductors exhibit unique advantages of earth abundance, low cost, facile synthesis, and inherent stability in PEC systems[3]. Among all, hematite (α-Fe$_2$O$_3$) is a promising candidate photoanode material for PEC water splitting because of its broad visible photo-response region, suitable valence band edge, and low cost[4,5]. However, the actual performance of hematite photoanodes remains far lower than its theoretical value owing to several critical shortcomings such as extremely short hole diffusion length (2−4 nm), low carrier mobility (<0.2 cm^2 V^{-1} S^{-1}), and sluggish oxygen-evolution kinetics[4,6]. To overcome these challenges, various modification strategies have been widely explored including

nano structuring[7,8], impurity doping (metallic or nonmetallic)[9,10], homojunction/heterojunction[11,12] and interface/surface modification[13,14] in order to improve the PEC performance.

Impurity doping is generally adopted to improve the poor conductivity of hematite, but the plateau photocurrent density (*J*$_{ph}$) of single photoanode is still far lower than its ideal value (~12.6 mA cm^{-2} for bandgap of 2.1 eV) owing to inherent shortcomings mentioned above. In addition, the intensified band bending caused by high-valence ion doping usually increases the onset potential (*V*$_{on}$) of the photocurrent[15]. A benign side effect was also reported in Ge doping into a hematite nanorod photoanode, which suppressed Sn diffusion from a F-doped SnO$_2$ (FTO) substrate, and recorded a remarkable *J*$_{ph}$ of ~3.5 mA cm^{-2} at 1.23 V$_{RHE}$[16]. However, there are few studies on the effect of impurity doping on absorption capability and transmittance characteristics of hematite films, which is essential for efficient unassisted

[1]College of Materials Science and Engineering, Sichuan University, Chengdu 610065, China. [2]Engineering Research Center of Alternative Energy Materials & Devices, Ministry of Education, Sichuan University, Chengdu 610065, China. [3]School of Energy and Chemical Engineering, Ulsan National Institute of Science and Technology (UNIST), 50 UNIST-gil, Ulsan 44919, Republic of Korea. ✉e-mail: jzchen@scu.edu.cn; jlee1234@unist.ac.kr; hmzhang@scu.edu.cn

solar water splitting in PEC and PV-PEC systems. Homojunction or heterojunction features extra space-charge region and built-in electric field, which effectively suppress carrier recombination especially in the bulk. For instance, Yi et al.[17] reported Co_3O_4/Ti:Fe_2O_3 $p-n$ heterojunction loaded with cobalt phosphate (Co-Pi) co-catalyst that showed a J_{ph} of 2.7 mA cm^{-2} and η_{bulk} of ~23.0% at 1.23 V$_{RHE}$, where p-type Co_3O_4 plays a key role in promoting charge separation. There are many other studies on hematite homojunctions and heterojunctions that enhance charge separation and overall PEC performances such as $n-n$ heterojunction of Ir_2O_3/Ti:Fe_2O_3[18], $p-n$ heterojunction of MoS_x/Ti:Fe_2O_3[19], and $p-n$ homojunction of Mg:Fe_2O_3/P:Fe_2O_3[20]. In previous reports, guest phase materials (n or p-type) were mostly pre-synthesized and coupled with the host hematite via solid-solid contact[21,22]. In this case, poor interactions and interfacial defects are inevitable, severely limiting the complete efficacy of the junctions. In stark contrast, in situ fabrication is an effective way to address these issues owing to strongly coupled interfaces and good lattice matching[23]. Besides, both impurity doping and junction construction are usually devoted to enhanced J_{ph} and bulk charge separation, but neither has much effect on surface charge separation[24,25], thus restricting its impact on improved PEC performance. Therefore, co-catalysts are generally applied to enhance surface charge separation, but with some negative side effects due to improper band edges or blocking light absorption[26]. Consequently, we need to develop multiple collaborative strategies that work synergistically to enhance the performance of photoelectrodes.

Fabricating a multi-junction (like $BiVO_4$/Fe_2O_3[27], WO_3/$BiVO_4$[28] or WO_3/Fe_2O_3[29]) or combining independent hetero-type photoanodes ($BiVO_4$‖Fe_2O_3[30]) are efficient for improving light harvesting via breaking the Shockley–Queisser limit of single junction (originally conceptualized on solar cells)[31]. However, several issues, including energy band and lattice matching of heterogeneous phases in a multijunction[27] and complicated arrangement among hetero-type photoanodes lead to the difficult realization of high performance for metal oxide photoanodes. In contrast, 'homo-type multiple photoelectrodes (HMP)' simply optimizes the individual single photoelectrode independently, and the performance of HMP becomes the simple sum of each one. In this system, transparency becomes an important parameter. Numerous studies have been implemented to reveal the potential application of HMP in a stack configuration, including Fe_2O_3[32], $BiVO_4$[33], CdSe[34] and TiO_2[35] photoanodes and Cu_2O[36] photocathodes. The hematite photoanode requires a relatively thick film to maximize the absorption of incident sunlight owing to its low absorption coefficient (~10^4 cm^{-1})[32], and the penetration depth of the light into hematite film can actually reach up to ~1500 nm to generate effective J_{ph}[37]. However, the extremely short hole diffusion length inevitably leads to severe carrier recombination in the thick film. These conflicting requirements for efficient hematite photoanodes can be reconciled effectively by constructing HMP with photoanodes of a suitable film thickness. If the optical transmittance and performance of hematite photoelectrode can be balanced in an optimized way, the huge gap between the actual and theoretical J_{ph} of hematite can be narrowed, which could enhance the potential of the multi-absorbers devices in terms of economic cost and system complexity.

In our previous works[38], hybrid microwave annealing (HMA) has been proven to be a highly powerful annealing technique to fabricate high-efficiency photoelectrodes because it allows the sample treated at a very high temperature for an extremely short time of a few minutes by using a good microwave absorber (e.g., graphite) as a susceptor. Thus, the short annealing time limits the sintering of the photoelectrode to preserve its nanostructure even under such a high temperature. In addition, it does not damage the FTO substrate, especially concerning the conductivity of tin oxide and transmittance of glass substrate, which are crucially required to construct highly transparent hematite photoanodes. It should also be noted that HMA produces some reductive gases like CO by partial combustion of the graphite susceptor, which definitely affects the valence state of the active component of the photoelectrode.

Here, we report a strategy for in situ construction of $p-n$ homojunction hematite photoanode via single antimony (Sb) doping by using HMA, which exhibits a remarkable J_{ph} of 3.33 mA cm^{-2} at 1.23 V$_{RHE}$ under simulated sunlight (100 mW cm^{-2}). Interestingly, Sb ions with lower than trivalent state (hereinafter Sb$^{<3+}$) were induced by HMA near the surface (within depth of ~3 nm) serving as an acceptor impurity for p-type hematite (Sb$^{<3+}$:Fe_2O_3), while pentavalent Sb ions (Sb^{5+}) were generated at the center of hematite serving as a donor impurity for n-type hematite (Sb^{5+}:Fe_2O_3), thereby forming an Sb$^{<3+}$:Fe_2O_3/Sb^{5+}:Fe_2O_3 (abbreviated as Sb$^{<3+}$:/Sb^{5+}:Fe_2O_3) $p-n$ homojunction spontaneously. The additional driving force from the built-in electric field of $p-n$ homojunction effectively suppresses charge recombination, especially in the bulk, showing a high bulk charge separation efficiency (η_{bulk}) of ~24.8% near its onset potential (~0.9 V$_{RHE}$) and ~51.3% η_{bulk} at 1.23 V$_{RHE}$, respectively. Note that the achieved η_{bulk} values are superior to the most advanced hematite photoanodes reported in the literature, thus representing a key breakthrough for hematite photoanodes. Moreover, $p-n$ homojunction photoanode with an optically transparent co-catalyst shows an additional enhancement of J_{ph} to 4.21 mA cm^{-2} at 1.23 V$_{RHE}$ owing to an increased surface charge separation efficiency ($\eta_{surface}$) of 88.3%. In particular, Sb doping strengthens the absorption capacity of hematite for high-energy photons (<450 nm) and apparently improves the optical transparency with a transmittance of 72% at 600 nm for the optimized Sb$^{<3+}$:/Sb^{5+}:Fe_2O_3 $p-n$ homojunction film. Moreover, HMA could prepare highly transparent electrodes by maintaining the transmittance because of little damage to the FTO substrate. Consequently, a parallel 6-stacked photoanode recorded a near-theoretical J_{ph} of ~10 mA cm^{-2} under standard PEC water splitting conditions. This parallel-connected stack of six hematite photoanodes with high performance could be a big step forward in the development of practical hematite photoelectrode for solar water splitting.

Results
Construction and microstructure of Sb$^{<3+}$:/Sb^{5+}:Fe_2O_3 $p-n$ homojunction

The synthesis procedure of Sb$^{<3+}$:/Sb^{5+}:Fe_2O_3 $p-n$ homojunction photoanode is shown in Fig. 1a (detailed procedure in Supplementary Fig. 1). The prepared Fe_2O_3 nanorods (annealed at 400 °C for 1 h) was spin-coated with a SbCl$_3$ solution (dimethoxyethane as a solvent) to obtain a conformal thin amorphous SbOCl layer as an Sb dopant source. Then, the sample was subjected to HMA for a few minutes to fabricate a Sb$^{<3+}$:/Sb^{5+}:Fe_2O_3 $p-n$ homojunction photoanode. Here, HMA plays a critical role in the successful synthesis of $p-n$ homojunction, which simultaneously provides a high annealing temperature (~1000 °C) and a reductive atmosphere required to form different valence states of Sb dopants. Most Sb^{3+} ions in SbOCl layer were actuated into hematite lattices to become Sb^{5+} ion dopants by the high temperature of HMA, whereas a part of the Sb^{3+} ions was reduced into Sb$^{<3+}$ ion dopants in the top several nanometers depth of hematite nanorods by reductive atmosphere of HMA. Finally, a transparent co-catalyst layer of NiCoFe(OOH)$_x$ was deposited on the surface of Sb$^{<3+}$:/Sb^{5+}:Fe_2O_3 to improve the charge carrier injection efficiency.

X-ray diffraction (XRD) patterns of $p-n$ homojunction hematite photoanodes are shown in Supplementary Fig. 2. The high SbCl$_3$ concentration broadens the (110) peak and decreases its intensity, indicating that the Sb doping lowers the crystallinity of hematite. Moreover, the 2θ position shifts to lower angles when the concentration is high enough, which is related to the formation of a possible new phase $Fe_2Sb_2O_7$ by HMA. Among the common $Fe_xSb_yO_z$ compounds (JCPDS no. 46-1387 for $FeSbO_4$; JCPDS no. 07-0349 for $FeSb_2O_6$; JCPDS no. 07-0065 for $Fe_2Sb_2O_7$), the $Fe_2Sb_2O_7$ (103) peak of is the closest to the Fe_2O_3 (110) and is expected to induce such shift of the Fe_2O_3 (110) peak. The formed SbOCl layer by spin-coated SbCl$_3$ solution could
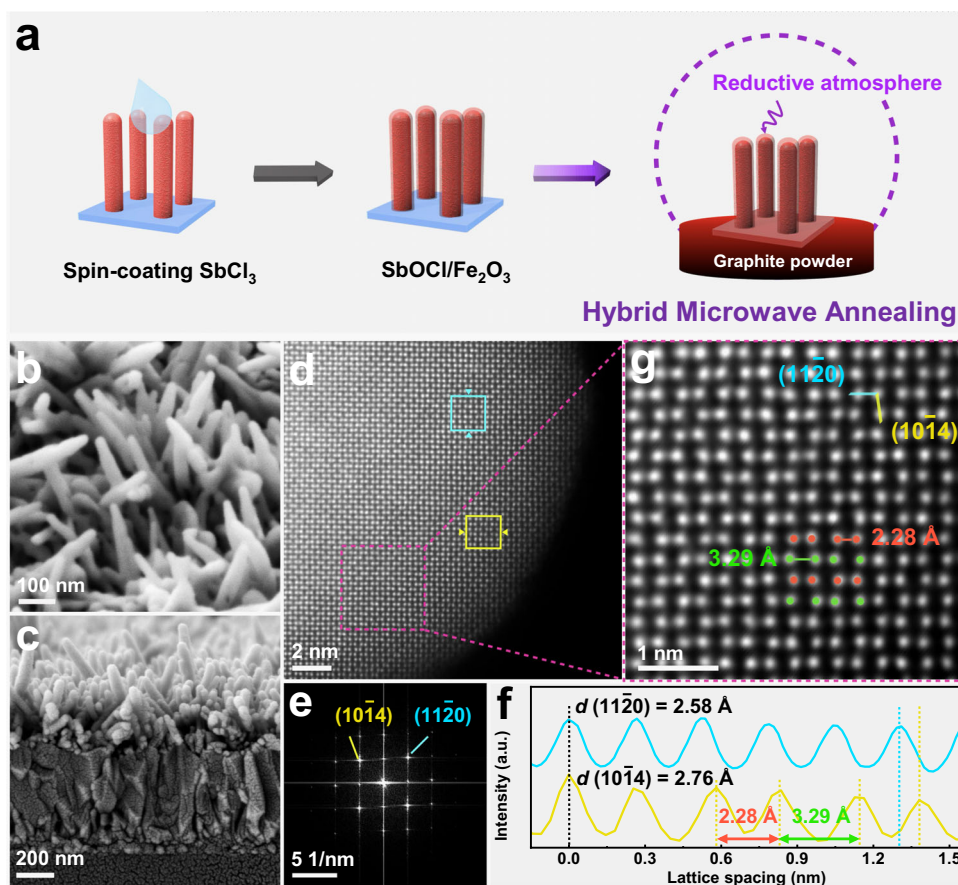
Fig. 1 | Construction and microstructure characterization of $Sb^{<3+}$:/Sb^{5+}:Fe_2O_3 nanorods. a Synthesis procedure. **b** SEM top and **c** cross-section view. **d** HAADF-STEM and corresponding **e** FFT images. **f** Integrated pixel intensities along the arrow directions in (**d**) (blue: (11$\bar{2}$0); yellow: (10$\bar{1}$4)). **g** Locally amplified HAADF-STEM image of (**d**).

protect nanorods during the HMA process, preserving the morphology of nanorods by suppressing aggregation (scanning electron microscopy (SEM) images in Supplementary Fig. 3). The synthesized $p–n$ homojunction nanorods exhibits a film thickness of ~400 nm with diameters of 30–50 nm (Fig. 1b, c), which were similar to those of less crystalline hematite nanorods before HMA treatment (Supplementary Fig. 4A). In contrast, the bare Fe_2O_3 nanorods are fused into big nanoparticles with a coralline shape at the bottom (Supplementary Fig. 3A). The well-preserved thin nanorods are beneficial to shortening hole diffusion length of hematite and enlarging contact area with the electrolyte. On the other hand, the surface of $p–n$ homojunction nanorods becomes smooth relative to that of the pristine, indicating that HMA could reconfigure the surface structure by the extremely high-temperature annealing (Supplementary Fig. 4A, B).

Cs-aberration-corrected high-angle annular dark-field scanning transmission electron microscopy (HAADF-STEM) in Fig. 1d shows a clear and ordered atomic arrangement, suggesting an excellent crystal structure with a low concentration of Sb doping. The energy-dispersive X-ray spectroscopy (EDS) analysis also indicates that Sb doping concentration is similar to that of Sn diffused from FTO (Supplementary Fig. 5). The crystal planes of the Fe_2O_3 nanorods were identified from the atomic stacking direction and the corresponding fast Fourier transform pattern, where two d-spacings of 2.76 and 2.58 Å corresponded to crystal planes of (10–14) and (11–20) of hematite, respectively, showing a single crystalline structure of hematite (Fig. 1d–f). Interestingly, not all atoms on each crystal plane are arranged neatly like previously reported in situ doped hematite by Ta[25] and Hf[39]. There is a shift in the position of atoms on (10–14) plane, which is related to the decreased crystallinity after Sb doping as reflected by the XRD pattern. As marked in Fig. 1f, g, the distance between metal atoms

increased to 3.29 Å and decreased to 2.28 Å, alternating with each other, which diverts from the standard d-spacing of ~2.76 Å. Similarly, Li et al.[40] reported the distortion of the position of cerium atoms in cerium dioxide that accompanies the evolution process of oxygen vacancies, which is concluded to benefit the rapid migration of O atoms. Here ex situ Sb doping has created a periodic structural distortion in the lattice of Fe_2O_3 (Fig. 1g), which is believed to change the surrounding electronic structure and potential field of atoms on (10$\bar{1}$4). It is known that electron transport along (10–14) plane is 4 orders of magnitude lower than that along (11$\bar{2}$0) plane[41], and such increased structural asymmetry is favorable for formation of small polaron and charge transport[42,43].

Characterization of $Sb^{<3+}$:/Sb^{5+}:Fe_2O_3 $p–n$ homojunction

Mott–Schottky (M–S) measurement, X-ray photoelectron spectroscopy (XPS), and ultraviolet photoelectron spectroscopy (UPS) are combined to identify the $p–n$ homojunction. The PN-x (x = 5, 10, 20, 40 mM, PN-x refers to the sample of Fe_2O_3 coated with different concentrations of $SbCl_3$) samples show the typical "V-shaped" M–S plots with the co-existence of positive and negative slopes (Fig. 2a), which provides direct evidence of $p–n$ homojunction[22,44]. With increasing $SbCl_3$ concentrations, the negative slope becomes larger, indicating that p-type domain over the outer part of the n-type hematite increases. Moreover, the crossing point of positive and negative slopes shows a positive shift, indicating the capacitance increase due to the extra space-charge region in the $p–n$ homojunction[45]. After oxidation, both negative slopes of PN-10-O and PN-40-O are weakened and even vanished (Supplementary Fig. 6), which indirectly demonstrates the existence of $Sb^{<3+}$ species. The donor density (N_D) of the optimized PN-10
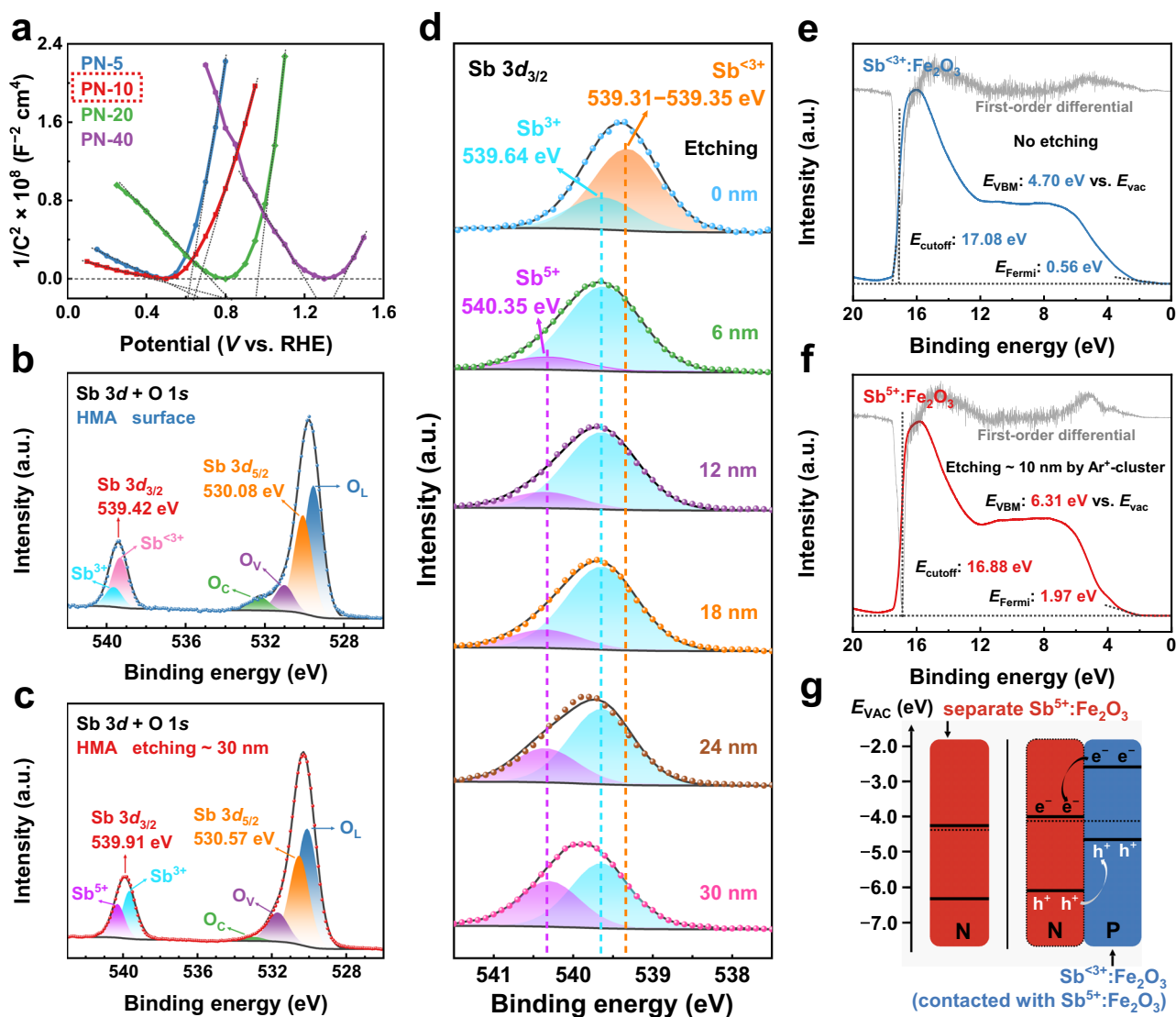
Fig. 2 | Characterization of Sb$^{<3+}$:Fe$_2$O$_3$/Sb^{5+}:Fe$_2$O$_3$ $p–n$ homojunction. a M–S plots of PN-x. **b** Sb $3d$ + O $1s$ XPS of PN-10 on the surface. **c** Sb $3d$ + O $1s$ XPS of PN-10 at etching depth of ~30 nm. **d** Sb $3d_{3/2}$ XPS depth profiles of PN-10 at different etching depths. UPS of PN-10 **e** on the surface and **f** inside. **g** Schematic diagram of band alignment of PN-10 homojunction.

photoanode was calculated to be 6.71×10^{19} cm^{-3}, and the validity of this M−S analysis was evaluated in Supplementary Fig. 7.

The identification of Sb oxidation states by XPS is a little complicated owing to the overlap of Sb $3d_{5/2}$ peak with O $1s$ peak. However, the Sb $3d_{5/2}$ peak can be separated from the overlapped Sb $3d$ + O $1s$ XPS spectra with reference to Sb $3d_{3/2}$. Binding energy difference (Δ_{BE}) between Sb $3d_{5/2}$ and Sb $3d_{3/2}$ in antimony oxides is generally fixed to 9.34 eV with an area ratio of 1.5[46,47]. We analyzed Sb $3d_{3/2}$ peak according to the standard fitting results of Sb$_2$O$_3$ (~539.64 eV for Sb^{3+}) and Sb$_2$O$_5$ (~540.35 eV for Sb^{5+}) in Loiudice's work (Supplementary Table 1)[47]. All the detailed fitting data of Sb $3d$ in this work are listed in Supplementary Table 2. Besides, a Sb:Fe$_2$O$_3$ sample prepared with the optimum 10 mM SbCl$_3$ was treated by conventional thermal annealing (CTA) for comparison (denoted as Sb:Fe$_2$O$_3$-CTA), of which Sb $3d_{3/2}$ and Sb $3d_{5/2}$ peaks at binding energies (BEs) of ~539.84 and ~530.50 eV (Supplementary Fig. 8A) are consistent with the results of previous reports[48]. Interestingly, PN-10 shows obvious shifts towards lower BEs relative to those of Sb:Fe$_2$O$_3$-CTA; Sb $3d_{3/2}$ peak from ~539.84 to ~539.42 eV and Sb $3d_{5/2}$ peak from ~530.50 to ~530.08 eV. Note that the Sb $3d$ BEs of PN-10 is even lower than those of Sb$_2$O$_3$ (Sb $3d_{3/2}$ at

~539.64 eV and Sb $3d_{5/2}$ at ~530.30 eV), indicating that the valence state of Sb dopants at the surface of PN-10 is less than 3+ (Fig. 2b). A series of PN-x samples prepared by x mM SbCl$_3$ solutions were compared in Supplementary Fig. 8B. However, the Sb$^{<3+}$ species disappeared completely when PN-10 was kept in a H$_2$O$_2$ solution (~30 wt%) due to reoxidation of Sb$^{<3+}$ back to Sb^{3+} and Sb^{5+} (denoted as PN-10-O) (Supplementary Fig. 8C, Supplementary Table 2).

Moreover, PN-10 was further subjected to XPS depth profiling to verify the successful formation of $p–n$ homojunction (Fig. 2c, d). At an etching depth of ~30 nm, Sb $3d_{3/2}$ and Sb $3d_{5/2}$ peaks are observed at BEs of ~539.91 eV and ~530.57 eV, respectively, which shows a composition of ~41% Sb^{5+} and ~59% Sb^{3+} ions, indicating that internal hematite is n-type. However, the amount of Sb^{5+} dopants shows an increasing gradient with the etching depth, probably due to the gradient diffusion of reductive CO, generating a stepwise band bending in n-type region. As schematically illustrated in Supplementary Fig. 9, it would promote separation and smooth flow of charge carriers in addition to the effect of $p–n$ junction[25].

The Fe $2p$ XPS spectra of all samples display Fe $2p_{1/2}$ (~724.1 eV) and Fe $2p_{3/2}$ (~710.6 eV) peaks accompanied by small satellite peaks of
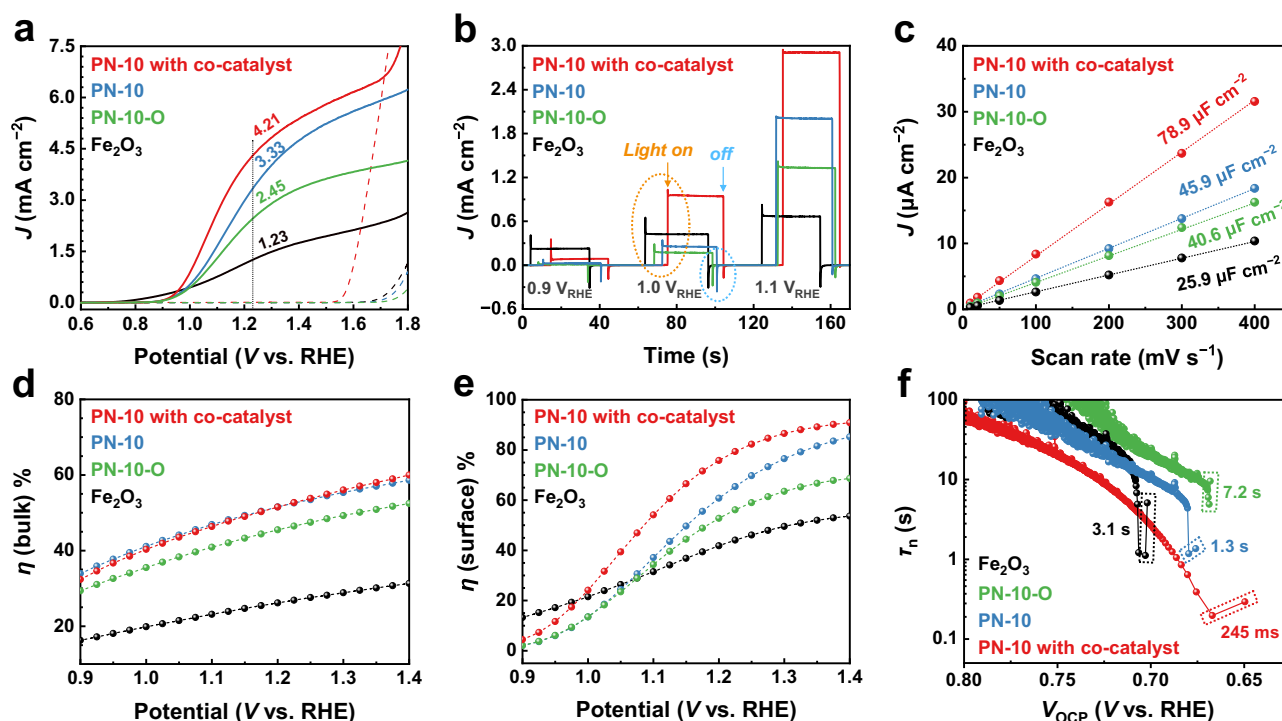
Fig. 3 | Photoelectrochemical performance of single photoanode. a J–V curves, **b** J–t curves under chopped illumination, **c** ECSA, **d** bulk and **e** surface charge separation efficiencies, and **f** OCP-derived carrier lifetimes of bare Fe_2O_3, PN-10-O, PN-10 and PN-10 with co-catalyst.

Fe^{3+} around 719 eV and Fe^{2+} around 716 eV[49]. Fe 2p peaks of PN-10 (Supplementary Fig. 10A) show a negative shift relative to that of $Sb:Fe_2O_3$-CTA (Supplementary Fig. 10B) and etched PN-10 (Supplementary Fig. 10C), along with a strongest Fe^{2+} satellite signal owing to the surface reduction induced by HMA. Besides, the depth-etched PN-10 also shows stronger Fe^{2+} satellite signal than that of the CTA sample. The results agree with the above O1s analysis (Supplementary Table 2), indicative of the good electrical conductivity by HMA. The Sn 3d XPS depth profiles (Supplementary Fig. 11) shows a gradient Sn diffusion in the PN-10 sample, which also contributes to the charge separation and flow. Note that Sb^{3+} is easier to be reduced under HMA because the dissociation energy of Sb–O bond is smaller than those of Fe–O and Sn–O bonds ($D°_{298}$/kJ mol^{-1} = Sb–O (372) < Fe–O (409) < Sn–O (528))[50].

From UPS in Fig. 2e, f, the valence band edges are determined to be −4.30 and −6.31 eV vs. vacuum level for surface $Sb^{<3+}$:Fe_2O_3 and internal Sb^{5+}:Fe_2O_3, respectively, which are obtained by subtracting the width of UPS spectrum from the excitation energy (21.22 eV). The big difference of E_{Fermi} (the valence band maximum with respect to E_F) between surface and inside (from 0.56 to 1.97 eV) demonstrates the existence of p–n homojunction in PN-10, which agrees well with its valence band XPS (VBXPS) measurements between surface and inside (from 0.63 to 1.73 eV) (Supplementary Fig. 12A, B). In addition, the bandgaps of PN-10 and PN-10-O are calculated to be 2.08 eV according to the ultraviolet-visible (UV–Vis) absorption spectra (Supplementary Fig. 13). Based on these analyses, the band alignment of $Sb^{<3+}$:Fe_2O_3/Sb^{5+}:Fe_2O_3 p–n homojunction is schematically illustrated in Fig. 2g, in which the band energy equilibrium of p–n junction was also taken into consideration.

Photoelectrochemical water oxidation over modified photoanodes

The PEC water oxidation performance of the synthesized photoanodes was evaluated under simulated sunlight (1 sun, 100 mW cm^{-2}) in a three-electrode configuration, which is composed of the photoanode as the working electrode, Ag/AgCl (3 M KCl) as the reference electrode,

and Pt mesh as the counter electrode, using 1 M NaOH solution as electrolyte (Supplementary Fig. 14). Figure 3a presents the photocurrent–potential (J–V) curves for hematite nanorod photoanodes subjected to different treatments. The optimized PN-10 sample achieves a high J_{ph} of 3.33 mA cm^{-2} at 1.23 V_{RHE} (Supplementary Fig. 15), which shows improvement by 2.0 and 1.7 times compared to $Sb:Fe_2O_3$-CTA (Supplementary Fig. 16) and bare Fe_2O_3 by HMA, respectively. This performance is superior or comparable to the leading hematite photoanodes doped with other elements (Supplementary Table 3). When PN-10 was sufficiently oxidized, the obtained PN-10-O showed a decreased J_{ph} of 2.45 mA cm^{-2} at 1.23 V_{RHE} owing to the extinction of p–n homojunction. By further modification of NiCoFe(OOH)$_x$ co-catalyst, the PN-10 photoanode achieves a notable J_{ph} of 4.21 mA cm^{-2} at 1.23 V_{RHE} (Supplementary Figs. 17 and 18), outperforming the 1.64 mA cm^{-2} of $Sb:Fe_2O_3$-CTA with the same co-catalyst (Supplementary Fig. 16).

The PN-10 photoanode shows the lowest V_{on} of 0.88 V_{RHE} among all PN-x photoanodes (Supplementary Fig. 15B), which is still larger than that of bare Fe_2O_3 (0.75 V_{RHE}) owing to the negative effect of doping[51]. Actually, the practical V_{on} of photoanodes is always more positive than its flat band potential (E_{FB}) owing to a required kinetic overpotential for oxygen-evolution reaction (OER)[52]. Generally, heavy surface doping affects the semiconductor/electrolyte interface and impairs the validity of M−S results for E_{FB} determination. Hence, a more accurate method of chopped illumination (CI) is proposed here, which is not compromised by substantial rates of Faradaic processes[53]. As shown in Supplementary Fig. 19, E_{FB} shifts positively with heavier doping of Sb, and all Sb-doped Fe_2O_3 samples show an increased difference (>320 mV) between V_{on} and E_{FB} relative to that of bare Fe_2O_3 (290−300 mV). However, PN-10 with optimum Sb doping concentration has the smallest overpotential (320−330 mV) among all Sb-doped Fe_2O_3 samples (370−380 mV for PN-5, 390−400 mV for PN-20, and 430−440 mV for PN-40). As shown in Fig. 1c, the PN-10 nanorod film is not fully dense, and the extremely high temperature of HMA would produce tiny cracks, leading to partial exposure of the current

collector. Therefore, PN-10 with co-catalyst modification improves its V_{on} to a limited extent due to the effect of shunting[54]. Generally, a better PEC performance of hematite photoanodes could be obtained in alkaline electrolyte than in neutral electrolyte owing to the reduced surface charge density and the coupling of adjacent surface trapped holes at higher pH[55]. Particularly, PN-10 shows a less positive shift of V_{on} than that of bare Fe_2O_3 (Supplementary Fig. 20), indirectly reflecting its existence of one or more lower energy barriers in the typical OER process[10,56].

Part of the photo-excited holes accumulated on the surface is injected into OER and generates steady J_{ph}, while the rest is lost owing to surface recombination. The $J–t$ curves under CI close to V_{on} exhibit dramatically reduced transient photocurrents upon light-on for the PN-10 photoanode relative to those of bare Fe_2O_3 and PN-10-O (Fig. 3b), indicating that hole loss on the surface was lessened because of the passivated surface. In contrast, the transient photocurrent of PN-10 upon light-off does not present this behavior, but instead shows apparently cathodic transient peaks similar to that of PN-10-O, indicating the recombination of the separated holes with electrons. This phenomenon was demonstrated to be related to the p-type transport behavior near to surface region[57]. Consequently, $p–n$ homojunction under light irradiation could provide additional driving force for charge separation and accelerate hole injection to mitigate hole accumulation. The amount of hole loss at different applied potentials can be calculated by chronoamperometry measurement under CI[58] (Supplementary Fig. 21). In Supplementary Fig. 21 F, the hole loss amount of PN-10-O is smaller than that of bare Fe_2O_3 owing to the enhanced conductivity on the surface after Sb doping, while PN-10 with surficial $Sb^{<3+}$ species further reduces the hole loss of recombination especially at potentials <1.3 V_{RHE}, which is indicative of more effective hole injection to OER, thus generating a higher steady J_{ph} (4.21 mA cm^{-2}) at 1.23 V_{RHE}. The NiCoFe(OOH)$_x$ co-catalyst serves as an OER booster to increase the hole injection efficiency. As shown in Fig. 3a, NiCoFe(OOH)$_x$ has no significant effect on the improvement of V_{on}. However, the amount of hole accumulation on the surface after NiCoFe(OOH)$_x$ loading on PN-10 at a potential close to V_{on} (0.9 V_{RHE}) is remarkably increased (Supplementary Fig. 21F), which implies the possible function of hole extraction of NiCoFe(OOH)$_x$ co-catalyst. When the applied potential increases, the hole loss of PN-10 with co-catalyst becomes much smaller than those of bare Fe_2O_3, PN-10-O, and PN-10 photoanodes, indicating its efficient hole injection and accelerated OER. It was previously reported that the metal oxide/(oxy) hydroxide could have beneficial roles of both hole collection and oxygen-evolution catalysis at the same time[59,60].

The electrochemically active surface area (ECSA) of different photoanodes with the same geometric area of 1 cm^2 was calculated by dividing the double-layer capacitance (C_{dl}) extracted from cyclic voltammograms (CV) by the specific capacitance of the active material under identical electrolyte conditions ($C_s = 40$ μF cm^{-2} in 1 M NaOH[61]) (Supplementary Fig. 22). In Fig. 3c, surface Sb doping increases the C_{dl} of bare Fe_2O_3 photoanode (25.9 μF) by more than 50%, 40.6 μF for PN-10-O and 45.9 μF for PN-10. PN-10 shows a little higher C_{dl} than PN-10-O, indicative of a possible role of $Sb^{<3+}$ species in providing additional active sites. Importantly, C_{dl} of PN-10 is remarkably increased to 78.9 μF by >70% after co-catalyst loading, which reveals the promotion of hole utilization by co-catalyst. Accordingly, the ECSA values for bare Fe_2O_3, PN-10-O, PN-10, and PN-10 with co-catalyst are determined to be 0.65, 1.02, 1.15, and 1.97 cm^2, respectively. The increased active area for electrochemical adsorption of ions demonstrates a great number of active sites for water oxidation.

Bulk (η_{bulk}) and surface ($\eta_{surface}$) charge separation efficiencies were determined in the same electrolyte with addition of Na_2SO_3 as a hole scavenger (Supplementary Fig. 23). In Fig. 3d, η_{bulk} of PN-10 achieves a notable value of ~52.7% at 1.23 V_{RHE} among recent reports (Supplementary Table 4), ~2 times higher than that of bare Fe_2O_3.

PN-10-O generates a little smaller η_{bulk} of ~46.5%, still much higher than that of bare Fe_2O_3. The high η_{bulk} values of PN-10 and PN-10-O are attributed to the gradient doping of Sb^{5+} and Sn^{4+} ions, and the additional driving force of in situ formed $p–n$ junction without interfacial defects. Doping and $p–n$ homojunction also reduce the photocurrent gap between front and back illumination, indicating improved bulk electron transport (Supplementary Fig. 24). As expected, η_{bulk} does not show any effect of co-catalyst loading. In Fig. 3e, $\eta_{surface}$ of both PN-10-O and PN-10 are much higher than that of bare Fe_2O_3, with an improvement over 27% at 1.23 V_{RHE} after surface Sb doping. Notably, different Sb ion valence states on the PN-10-O and PN-10 surfaces generate different surface charge separation efficiency. $\eta_{surface}$ of PN-10 is almost the same as that of PN-10-O at low potentials (0.9–1.05 V_{RHE}), while it starts to exceed when applied potential increases further, indicating that $Sb^{<3+}$ species plays an important role at high applied potentials (especially for potentials over 1.23 V_{RHE}). With co-catalyst modification, however, $\eta_{surface}$ is improved in the whole potential range owing to more efficient hole extraction and utilization, reaching ~80% at 1.23 V_{RHE} and ~90% at 1.4 V_{RHE}.

The OER proceeds mainly via surface states and direct transfer from the valence band at moderately and highly anodic potentials in the PEC cells, respectively[62]. Iandolo and Hellman used first-principle calculations to investigate surface states on hematite under photoelectrochemical conditions and further demonstrated that increasing the potential could empty the surface states[63], which explains why the J_{ph} of water photo-oxidation increases slowly (smaller slope of $J–V$ curves) with the increase of potential. With the increase of applied potential, the surface states will gradually fade at about 1.1 V_{RHE} (V_1) until they reach a certain potential (V_2) where the surface states are completely emptied (Supplementary Fig. 25). The difference of potentials ($\Delta V = V_2 – V_1$) can reflect the surface-state density for different samples to a certain extent. ΔV of bare Fe_2O_3 is determined to be 356 mV, while those of PN-10-O and PN-10 increase to over 500 mV. The increased ΔV after Sb doping suggests that extrinsic doping via surface spin-coating method and post-annealing indeed increases the surface states of Fe_2O_3, which results in more positive V_{on} of PN-10-O and PN-10, consistent with the general understanding of doping effects. Notably, with the presence of $Sb^{<3+}$ species on the surface, different surface composition and electronic structure of PN-10 result in a reduced surface-state density compared to that of PN-10-O (ΔV: PN-10 vs. PN-10-O, 521 mV vs. 583 mV), which contributes to the enhanced surface charge separation and higher J_{ph} of PN-10. After co-catalyst modification, ΔV of PN-10 increases to 555 mV owing to the hole extraction function of NiCoFe(OOH)$_x$ co-catalyst as mentioned above (Fig. 3a).

The steady-state photoluminescence spectroscopy (PL) helps to reflect the lifetime of the photo-generated carrier. As reported in previous work, the PL spectrum of hematite photoanode has two emission peaks, one at ~590 nm and a stronger one at ~612 nm[64]. In Supplementary Fig. 26, PN-10 shows a reduced PL intensity compared to bare Fe_2O_3 and PN-10-O, which indicates that the carrier lifetime before recombination is prolonged after the formation of $p–n$ junction. Moreover, the open circuit potential (OCP) transient decay profiles provide additional information on the behaviors of the photo-generated carrier[17,65]. The fast OCP decay from illumination to a dark state generates a photovoltage ($\Delta OCP = OCP_{dark} – OCP_{light}$) that reflects the ability of charge separation. As shown in Supplementary Fig. 27, PN-10 exhibits an accelerated OCP decay relative to those of bare Fe_2O_3 and PN-10-O, which is further improved by loading NiCoFe(OOH)$_x$. The additional driving force to enhance charge separation confirms the effectiveness of the $p–n$ homojunction and the co-catalyst. The electron lifetime is derived from a general free electron recombination rate. In Fig. 3f, the carrier lifetime at the transient of $p–n$ homojunction is ~1.3 s, much shorter than those of bare Fe_2O_3 (~3.1 s) and PN-10-O (~7.2 s), and further decreases to ~245 ms with
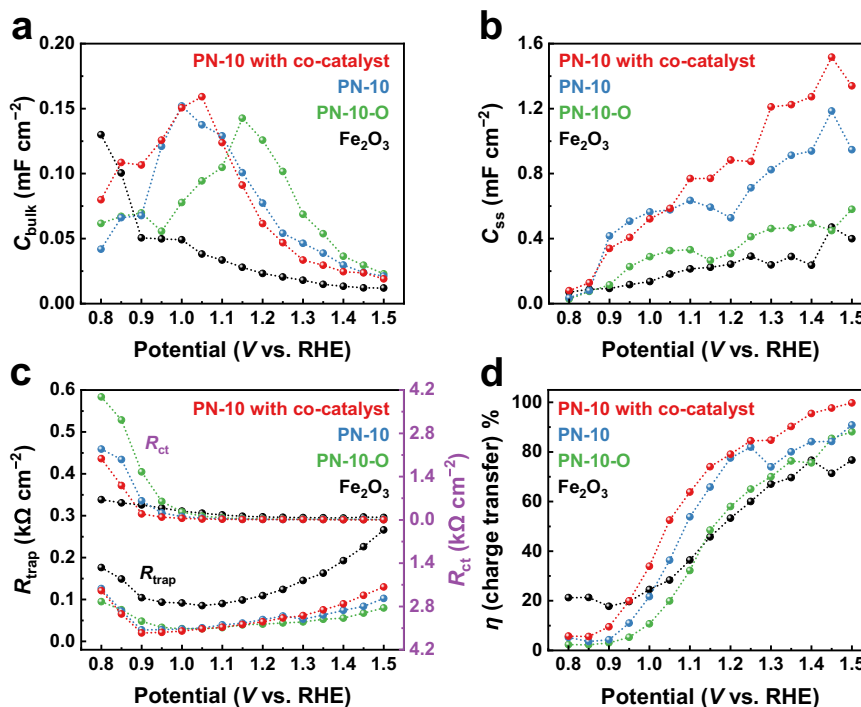
Fig. 4 | PEIS of bare Fe_2O_3, PN-10-O, PN-10, and PN-10 with co-catalyst photoanodes. a Bulk capacitance, **b** surface-state capacitance, **c** trapping and charge transfer resistance, and **d** charge transfer efficiency.

co-catalyst loading. The short transient lifetime corresponds to a fast charge recombination, indicating that the charge trapping is insignificant under illumination[17,66].

Photoelectrochemical impedance spectroscopy (PEIS) at different potentials from 0.8 (close to V_{on}) to 1.5 V_{RHE} (with a step of 50 mV) reveals the trends of capacitances and resistances, which provide insights into the contribution of gradient Sb doping, $p-n$ homojunction and co-catalyst to PEC performance (Supplementary Fig. 28). The obtained data were fitted to a typical two-RC-unit equivalent circuit model to decouple charge trapping and charge transfer resistances (Supplementary Table 5). In Fig. 4a, the maximum capacitances in the bulk (C_{bulk}) of PN-10-O, PN-10, and PN-10 with co-catalyst reach up to 4 times that of bare Fe_2O_3, which is ascribed to the additional driving force provided by gradient dopants of Sb^{5+} and Sn^{4+} ions. Moreover, the additional driving force results in an obvious peak of C_{bulk} values at the potential range of 1.0−1.15 V_{RHE}, where C_{bulk} initially increases at a remarkable rate and declines rapidly when applied potential further increases due to the enhanced charge extraction and the lower accumulation of photo-generated holes[67,68]. However, this behavior cannot be observed on bare Fe_2O_3, where C_{bulk} of bare Fe_2O_3 shows rapid decay in the whole potential range. Notably, the potentials of maximum C_{bulk} value for $p-n$ homojunctions (PN-10 and PN-10 with co-catalyst) are smaller than that of PN-10-O by 100−150 mV, indicating that the $p-n$ homojunction can effectively separate the photo-generated electron and hole with a small bias. The surface-state capacitance (C_{ss}) of PN-10-O with surface composition of "Sb^{5+} + Sb^{3+}" slightly increases compared to that of bare Fe_2O_3, while C_{ss} of PN-10 increases to ~2 times that of PN-10-O by surface composition of "$Sb^{<3+}$ + Sb^{3+}" (Fig. 4b). The higher C_{ss} comes from the contribution of the surface $Sb^{<3+}$ species, which helps to reduce charge recombination as mentioned above. The additional co-catalyst modification further enhances C_{ss} at potentials higher than water oxidation potential (1.23 V_{RHE}), indicating a notable contribution of co-catalyst to OER.

Figure 4c shows that trapping resistance (R_{trap}) values of PN-10-O, PN-10, and PN-10 with co-catalyst decrease greatly relative to that of bare Fe_2O_3 in the whole potential range of 0.8−1.5 V_{RHE} owing to the

enhanced bulk separation efficiency by high-valence doping effect. With the increase of potential, the charge transfer resistance (R_{ct}) of all Sb-doped photoanodes decreases owing to the enhanced surface conductivity. At a potential of 0.9 V_{RHE} close to V_{on}, R_{ct} of PN-10-O is still much higher than that of bare Fe_2O_3, while R_{ct} of PN-10 and PN-10 with co-catalyst are comparable or even lower than that of bare Fe_2O_3. The huge different R_{ct} values near V_{on} of PN-10-O and PN-10 reflect the beneficial role of surface $Sb^{<3+}$ species, which eventually enables higher J_{ph}.

Charge transfer through surface states is assumed as the predominant mechanism for surface charge transfer of OER[62], which determines the rate of water oxidation on photoanodes. The charge transfer and trapping rates are related to their corresponding charge transfer and trapping resistances extracted from PEIS. Further, the charge transfer efficiency (η_{ct}) can be estimated through the equation[69,70]:

$$\eta_{ct} = \frac{k_{ct}}{k_{ct} + k_{trap}} = \frac{R_{trap}}{R_{ct} + R_{trap}} \tag{1}$$

where k_{ct} and k_{trap} are the rate constants of charge transfer and trapping, respectively. η_{ct} in a wide potential range from V_{on} to 1.5 V_{RHE} are calculated in Fig. 4d to reflect the relationship between charge transfer and photocurrent density. The η_{ct} value of PN-10-O remains lower than that of bare Fe_2O_3 at potentials <1.15 V_{RHE} and becomes only a little better at higher potentials. At ~1.0 V_{RHE}, however, η_{ct} of PN-10 starts to exceed that of bare Fe_2O_3 and increases up to ~80% at 1.23 V_{RHE}. The turning potential of 1.0 V_{RHE} is consistent with the potential at which J_{ph} of PN-10 exceeds that of bare Fe_2O_3. Therefore, these results indicate that high J_{ph} of PN-10 is generated by the contribution of surface $Sb^{<3+}$ species instead of Sb^{3+} or Sb^{5+} ions. Further, co-catalyst modification enhances η_{ct} of PN-10 at all potentials.

In a 5 h stability test (Supplementary Fig. 29), PN-10 loses some of its stability relative to bare Fe_2O_3 (79.1%→74.2%) owing to the oxidation of p-type phase by surface trapped holes[71]. With co-catalyst modification, however, the stability of $p-n$ homojunction is greatly improved to
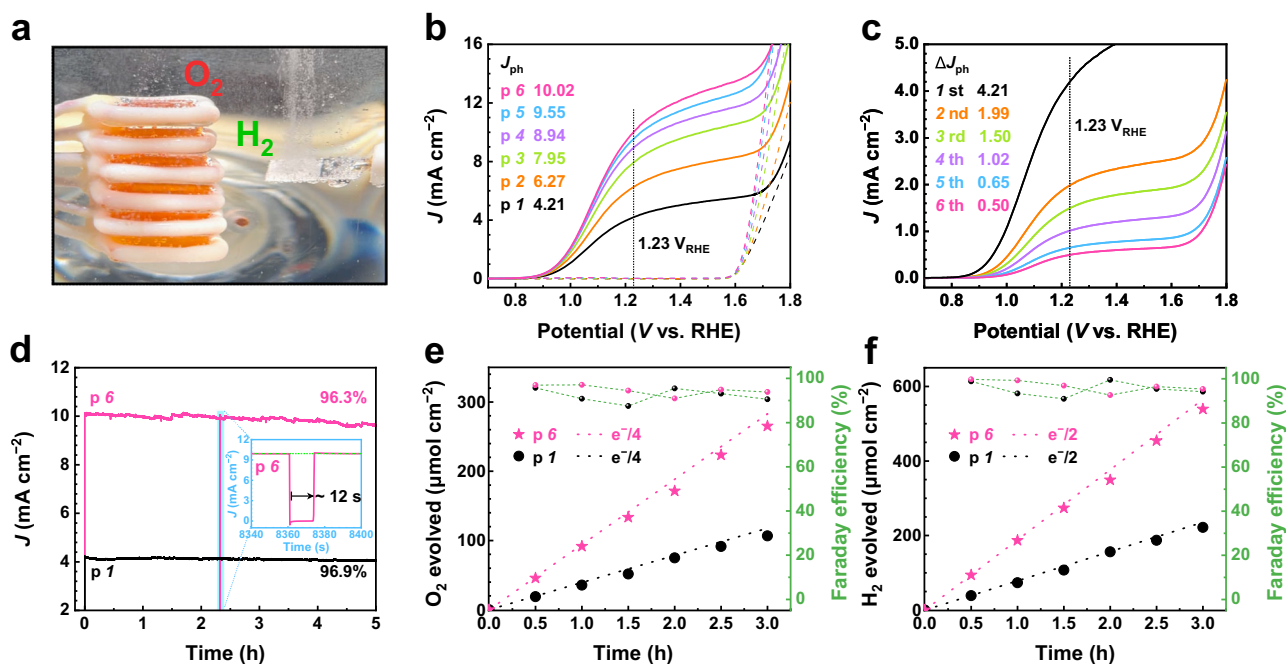
Fig. 5 | Photoelectrochemical performance of parallel multi-stacked photoanode using co-catalyst-loaded PN-10 films. a Schematic of a parallel 6-stacked photoanode at work. *J–V* curves of **b** parallel *n*-stacked (*n* = 1, 2, 3, 4, 5 and 6) photoanodes and **c** the *i*th (*i* = 1, 2, 3, 4, 5, and 6) photoanodes in 6-stacked configuration. **d** Stability of single PN-10 and parallel 6-stacked photoanode. **e** O_2 and **f** H_2 evolution from PEC water splitting of photoanodes at 1.23 V_{RHE}.

~96.9% due to the enhanced hole extraction and accelerated OER kinetics by the NiCoFe(OOH)$_x$ co-catalyst, which protects the *p*-type Sb$^{<3+}$:Fe$_2$O$_3$ layer and stabilizes the surface structure as illustrated in Supplementary Fig. 30. Additionally, the small energy gap between conduction band minimum (CBM) of Sb$^{<3+}$:Fe$_2$O$_3$ and valence band maximum (VBM) of Sb^{5+}:Fe$_2$O$_3$ determined by UPS and VBXPS indicates that some charge carriers tend to recombine owing to the coupling of CBM of Sb$^{<3+}$:Fe$_2$O$_3$ and VBM of Sb^{5+}:Fe$_2$O$_3$. With co-catalyst loading, however, the photo-generated holes arriving at the surface Sb$^{<3+}$:Fe$_2$O$_3$ layer can be injected into OER immediately, thus preventing hole recombination with VBM electrons of Sb^{5+}:Fe$_2$O$_3$ and inactivation of the surface Sb$^{<3+}$ species. This will give rise to a remarkable J_{ph} increase with co-catalyst modification.

Parallel multi-stacked *p-n* homojunction photoanodes
Interestingly, the transparency of the hematite photoanode film was improved by Sb doping under both treatments of CTA and HMA (Supplementary Fig. 31A, B). However, PN-10 by HMA exhibited a better transmittance than Sb:Fe$_2$O$_3$-CTA, especially in the long-wavelength region (>450 nm). For example, the transmittance of PN-10 at 600 nm (72%) is higher than that of Sb:Fe$_2$O$_3$-CTA (61%) (Supplementary Fig. 31C), which results from the well-preserved individual nanorods under HMA instead of severe aggregation under CTA. Besides, the hematite nanorod film prepared by HMA was dense at the bottom layer (~150 nm) but sparse in the upper layer (~250 nm), thereby enabling a better light penetration (Supplementary Fig. 32). Moreover, HMA-treated FTO does not show conductivity decrease of conductive F:SnO$_2$ layer and transparency loss of glass substrate, while the resistance of CTA-treated FTO (FTO-CTA) is doubled and the transmittance at 600 nm is reduced (Supplementary Fig. 33). On the other hand, loading the NiCoFe(OOH)$_x$ co-catalyst on *p−n* homojunction does not affect light absorption and transmittance (Supplementary Fig. 34). In fact, the penetration depth of light into hematite film can reach up to ~1500 nm to generate effective J_{ph}[37]. The high transparency and the long light penetration depth of the PN-10 film make it

an outstanding candidate for fabricating a parallel multi-stacked photoanode, which is a promising robust system for on-site energy production[35,72].

HMP of hematite utilizes the transmitted light from the preceding photoanodes at succeeding ones[34], and the thermalization loss could also be minimized since photons with energy in excess of E_g lose a part of their energy by emitting phonons via lattice vibrations and heat[31]. The fabricated 6 photoanodes show an average J_{ph} of ~4.11 mA cm^{-2} at 1.23 V_{RHE}, indicative of good reproducibility of the HMA-prepared *p−n* homojunction photoanodes (Supplementary Fig. 35). Parallel *n*-stacked (*n* = 1, 2, 3, 4, 5 and 6) photoanodes were fabricated using co-catalyst-loaded PN-10 films to obtain J_{ph} at 1.23 V_{RHE} of 4.21, 6.27, 7.95, 8.94, 9.55, and 10.02 mA cm^{-2} under standard conditions, respectively (Fig. 5a, b). In particular, the parallel 6-stacked photoanode records J_{ph} of over 10 mA cm^{-2}, which is by far closest to the theoretical value of a single hematite photoanode (12.6 mA cm^{-2}), which is a notable improvement for hematite photoanodes and is also superior to other multi-stacked photoelectrodes (see Supplementary Table 6 for benchmarking). We fabricated a three-electrode cell based on this kind of stack configuration that could perform overall water splitting under simulated sun illumination (Supplementary Movie 1). The measured J_{ph} of the *i*th (*i* = 1, 2, 3, 4, 5 and 6) photoanode in 6-stacked configuration shows 4.21, 1.99, 1.50, 1.02, 0.65, and 0.50 mA cm^{-2} at 1.23 V_{RHE} under standard condition, respectively (Fig. 5c), representing each contribution, which also demonstrates that sixth one is almost maximum owing to its very limited contribution. All the measured current densities match the theoretical results well (Supplementary Fig. 36). Note that the total sum of J_{ph} from these individual photoanodes is 9.87 mA cm^{-2}, almost the same as the measured 6-stacked configuration (10.02 mA cm^{-2}), which demonstrates the effective contribution of each photoanode. Owing to the superior stability of the single PN-10 photoanode with co-catalyst, the 6-stacked photoanode maintains ~96.3% of its initial activity in 5 h (Fig. 5d). A short video of 6-stacked photoanode operation is available as Supplementary Video 1. The gases 2H$_2$ + O$_2$ evolved from 6-stacked photoanode and Pt
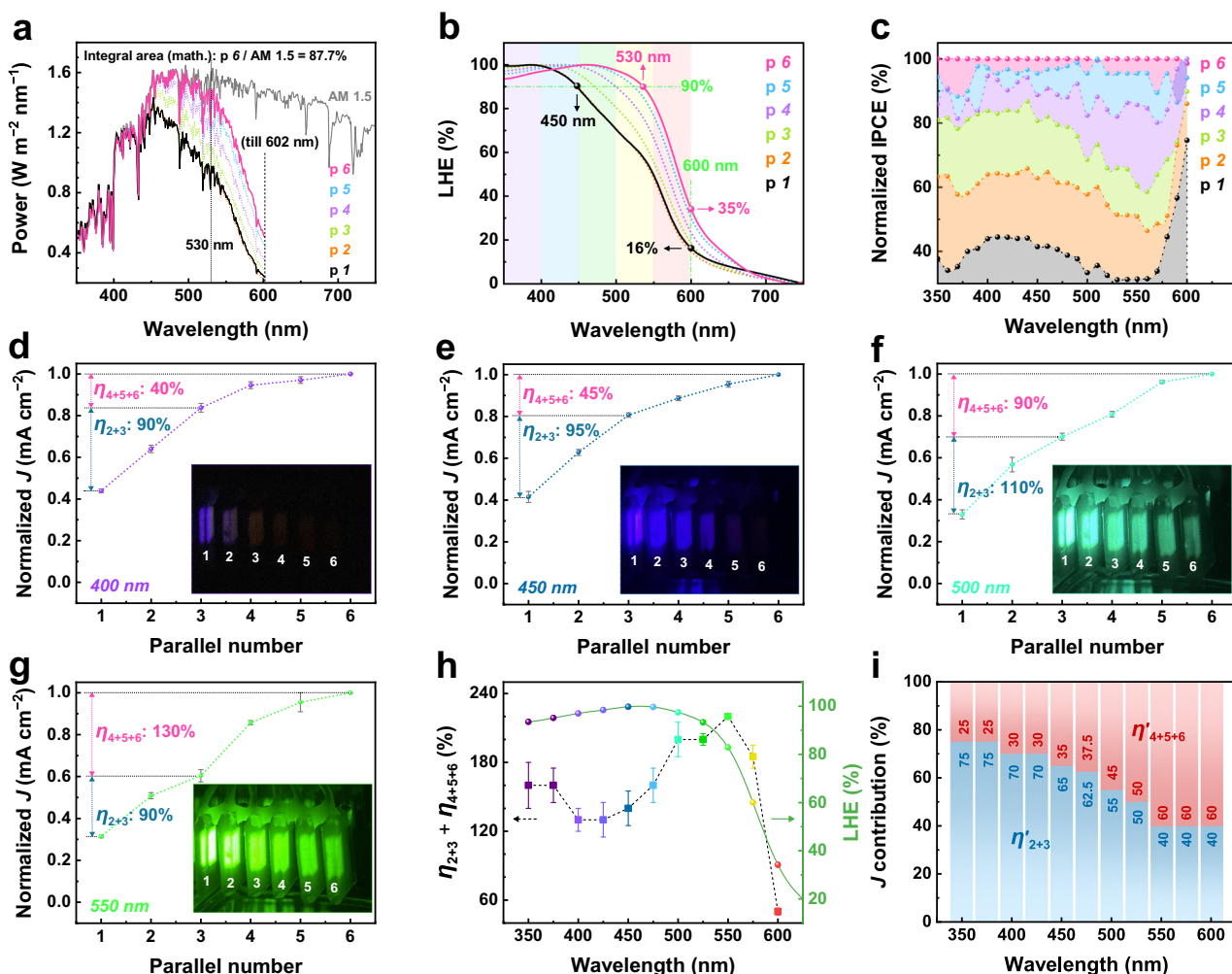
Fig. 6 | Light utilization of parallel multi-stacked photoanode using co-catalyst-loaded PN-10 films. a Light utilization in AM 1.5 G spectrum, **b** light-harvesting efficiency (LHE), **c** normalized IPCEs at 1.23 V_{RHE}, **d**–**g** normalized photocurrents at 1.23 V_{RHE} at specific wavelengths (insets are their optical images) of parallel n-stacked (n = 1, 2, 3, 4, 5 and 6) photoanodes. **h** η_n variation of 6-stacked photoanode at different wavelengths. The standard deviation (SD) is added to **d**–**h** to reflect the fluctuation of the measured photocurrent. **i** Contribution of J_{2+3} and J_{4+5+6} photoanodes.

photocathode were quantified by gas chromatography for 180 min, and most of the photocurrents came from water splitting with over 90% Faradaic efficiency (Fig. 5e, f).

UV–Vis absorption and incident photon-to-current conversion efficiency (IPCE) were used to explore the characteristics of light utilization in HMP. The optimized single PN-10 loaded with the NiCoFe(OOH)$_x$ co-catalyst film exhibits a high transmittance of ~72% at a wavelength of 600 nm, indicating that about 72% of the incident light remains available for the second absorber in HMP (Supplementary Fig. 37A). For dual photoelectrodes, roughly 40% of the incident light still passes through, indicating the potential for further effectiveness with more photoanodes. UV–Vis spectra of n-stacked photoanodes (Supplementary Fig. 37B) illustrate the absorption characteristics in the stack configuration. A notable increase in absorbance in the short-wavelength region (<450 nm) is observed in the preceding three photoanodes, with a clear rise of absorption in the long-wavelength region (>450 nm) in all succeeding ones. Consequently, the preceding three absorbers yield a J_{ph} of up to ~8 mA cm^{-2}, providing a helpful reference for hematite photoanodes in comparison with previous reports. The succeeding three photoanodes ultimately boost J_{ph} to ~10 mA cm^{-2} by utilizing the absorption of low-energy photons in the long-wavelength region.

In Fig. 6a, the light utilization of the parallel 6-stacked photoanode is almost 100% at wavelengths <530 nm in the AM 1.5 G spectrum. Within the theoretical absorption range (up to 602 nm for E_g of 2.08 eV), the parallel 6-stacked photoanode enhances light utilization efficiency to a high level of 87.7% according to the AM 1.5 G spectrum by mathematical integral area ratio (p 6/AM 1.5 G = 87.7%). In addition, the light-harvesting efficiencies (LHEs) of n-stacked photoanodes in Fig. 6b show that the single photoanode achieves LHEs of over 90% only for the absorption of short-wavelength light (<450 nm), while the 6-stacked photoanode extends the region to ~530 nm, which is close to its theoretical absorption edge. Particularly, the LHE of the 6-stacked photoanode near the absorption edge of 600 nm can still reach up to 35%, more than twice that of a single photoanode (16%). This UV–Vis absorption characteristic convincingly demonstrates that hematite HMP could provide its near-theoretical solar conversion efficiency.

The IPCE measurement was performed in a three-electrode PEC cell equipped with a monochromator (Supplementary Figs. 38 and 39A). The optimized single photoanode yields a maximum IPCE of only ~35% in the 350–400 nm range owing to a relatively low absorption coefficient (~10^4 cm^{-1}). However, the IPCE of the 6-stacked photoanode increases to ~85% in this region by the transmitted light through preceding electrodes. The IPCE value drops sharply beyond 400 nm due

to hematite's indirect band transition[73], yet >50% of the solar energy exploitable lies in this region, contributing to J_{ph}[30]. Figure 6c shows the normalized IPCEs of multi-stacked photoanodes at wavelengths of 350–600 nm. At long wavelengths (450–600 nm), the succeeding 4th, 5th, and 6th photoanodes in the stack still enhance the IPCE values considerably and contribute to the high J_{ph} of the 6-stacked photoanode. The IPCE increase of the 6-stacked photoanode relative to that of a single one is 130%, 140%, 200%, and 220% at 400, 450, 500, and 550 nm, respectively (Supplementary Fig. 38A). Even at the absorption edge (600 nm), the IPCE also increases by 50%. Moreover, the integrated IPCE concerning the AM 1.5 G spectrum at 1.23 V_{RHE} yields a solar photocurrent density (J_{sc}) of 9.89 mA cm^{-2} for the 6-stacked photoanode (Supplementary Fig. 38B), which is consistent with the experimentally measured value at 1.23 V_{RHE} (-10 mA cm^{-2}) (Fig. 5b). The remarkable enhancement of light absorption and IPCE in the long-wavelength region demonstrates the vital function and effectiveness of HMP, explaining the near-theoretical J_{ph} by the parallel 6-stacked photoanode.

For a deeper understanding, the normalized J_{ph} of n-stacked photoanodes excited by diverse monochromatic lights (ranging from 400 to 550 nm, at intervals of 50 nm) are shown in Fig. 6d–g, with additional details in Supplementary Fig. 39B–H. Clearly, all monochromatic lights effectively reach the last photoanode and generate J_{ph} (inset of optical images), indicating favorable transparency for each photoanode and the effectiveness of the stack configuration. The J_{ph} gain (%) increases with the wavelength in the range of 350 to 550 nm, while it rapidly decays as the wavelength approaches the absorption edge of 550–600 nm (Fig. 6h, Supplementary Fig. 39B–H). Notably, LHEs of the 6-stacked photoanode in the range of 350 to 525 nm are all over 90%, and the LHE at 550 nm is still over 80%, resulting in a near-theoretical photocurrent density. Further, the percentage of J_{ph} gain (η) at a specific wavelength can be described by the equation: $\eta_n = J_n/J_1$ (n = 2 + 3, or 4 + 5 + 6), where J_1 is the J_{ph} of the first photoanode, and J_{2+3} and J_{4+5+6} are the J_{ph} from the combination of 2nd and 3rd, and the combination of 4th, 5th, and 6th photoanodes, respectively. Due to the better utilization ability of high-energy photons (P_H) than low-energy photons (P_L), the preceding three photoanodes have absorbed the majority of P_H, while the succeeding three ones primarily absorb P_L for supplementation. In Fig. 6d–g, the η_{2+3} exhibits almost consistent values at different wavelengths, implying that the increasing J_{ph} gain of the 6-stacked photoanode arises from the joined J_{4+5+6} for supplementary absorption in the long-wavelength region. In detail, the η_{4+5+6} shows a greater enhancement with the increase of wavelengths, suggesting that the stack configuration works wonders at utilizing lower energy photons. The contributions of J_{2+3} and J_{4+5+6} at different wavelengths are presented in Fig. 6i. In the stack, J_{2+3} is committed to absorbing P_H and provides over 70% photocurrents at wavelengths of <425 nm, while J_{4+5+6} is committed to absorbing P_L and provides over 50% photocurrents at wavelengths of >525 nm.

Discussion

Extrinsic Sb doping induced by HMA has proved to be a promising approach for preparing efficient and transparent hematite photoanodes. A Sb$^{<3+}$:/Sb^{5+}:Fe$_2$O$_3$ p–n homojunction was constructed in situ successfully on hematite nanorods, achieving a remarkable J_{ph} of 3.33 mA cm^{-2} and a high η_{bulk} of 51.3% at 1.23 V_{RHE}. This outstanding performance resulted from enhanced charge separation in the bulk of hematite photoanode by gradient doping of Sb^{5+}/Sn^{4+} ions, and formation of a p–n homojunction. The surface p-type Sb$^{<3+}$:Fe$_2$O$_3$ was generated from the reductive atmosphere created by insufficient burning of graphite powder during the HMA process, while the generation of n-type Sb^{5+}:Fe$_2$O$_3$ was ascribed to Sb diffusion and oxidation by the high temperature of HMA. With NiCoFe(OOH)$_x$ co-catalyst loading, p–n homojunction photoanode further increased J_{ph} to 4.21 mA cm^{-2} and enhanced $\eta_{surface}$ to 88.3% at 1.23 V_{RHE}, which is

superior or comparable to the state-of-the-art hematite photoanodes reported recently.

The Sb doping into hematite improved film transparency, while the HMA technique minimized conductivity reduction of F:SnO$_2$ conductive layer and transparency loss of glass in the FTO substrate, which are meaningful attributes to move forward beyond the single Fe$_2$O$_3$ photoanode. Consequently, a parallel 6-stacked photoanode was assembled to boost light harvesting efficiency, particularly for low-energy photon utilization, achieving over 90% LHE across most of the theoretical absorption spectral range and a notable J_{ph} of -10 mA cm^{-2} close to the theoretical solar conversion efficiency of hematite (12.6 mA cm^{-2}) under standard PEC water splitting conditions. Thus, HMPs presented herein represent a significant step forward en route to practical solar hydrogen production using low-cost hematite-based photoanodes.

Methods

Construction of p−n homojunction hematite nanorods on FTO

The bare β-FeOOH nanorods were synthesized on an FTO (TEC8, 6–9 Ω, Pilkington) substrate using a simple hydrothermal method. First, a piece of 25 × 25 mm^2 FTO glass was ultrasonically cleaned in deionized water, ethanol, and acetone to ensure a hydrophilic surface. The cleaned substrate was then immersed in a 50 mL aqueous solution containing 0.15 M ferric chloride hexahydrate (FeCl$_3$·6H$_2$O, Aladdin, 99.0%), 1 M sodium nitrate (NaNO$_3$, Aladdin, 99.0%), and 200 μL nitric acid (HNO$_3$, Aladdin, 50%) and heated at 100 °C for 2 hours to grow a thin film of β-FeOOH nanorods. After rinsing with deionized water, the film was heated at 400 °C in air for 1 hour to convert the oxyhydroxide into hematite. Next, 100 μL of SbCl$_3$ solution at varying concentrations was applied to the 25 × 25 mm^2 hematite films. The films were spin-coated at 500 rpm for 10 seconds and 3000 rpm for 60 seconds, then dried at 60 °C for a few minutes. Finally, the dried samples were annealed for 2 minutes in a standard microwave oven (2.45 GHz, 1000 W) at full power, using graphite powder in a 100 mL Pyrex beaker as a microwave susceptor.

Co-catalyst modification

For ternary co-catalyst NiCoFe(OOH)$_x$ modification, the prepared photoanode was immersed into a mixed aqueous solution containing 5 mM nickel chloride hexahydrate (NiCl$_2$·6H$_2$O, Aladdin, 99.0%), cobalt chloride hexahydrate (CoCl$_2$·6H$_2$O, Aladdin, 99.0%) and FeCl$_3$·6H$_2$O for different durations (5, 10, and 20 min) at room temperature. Subsequently, the photoanode was dipped into 1 M NaOH immediately for several seconds to form oxyhydroxides.

Fabrication of parallel multi-stacked photoanodes

The exposed side of the FTO substrate was connected to a copper wire, and the geometric surface area of each prepared photoanode (1 × 1 cm^2) was defined, with all other conductive areas covered using epoxy resin (Scotch-Weld), cured at room temperature for 3 hours. Multiple Fe$_2$O$_3$ photoanodes were arranged in parallel and vertical alignment, and attached with epoxy resin. The spacing between each hematite photoanode was set to 0.2 cm.

Physical characterization

XRD patterns were collected using an Empyrean XRD system with Cu-K_α radiation (λ = 1.5406 Å) at 40 kV and 40 mA. The morphology and EDS were examined with an SEM (Zeiss Sigma 300). High-resolution scanning transmission electron microscopy, HAADF-STEM, and EDS mappings were performed using an FEI Themis Z microscope. XPS (Kratos Axis Ultra^{DLD}, Al K_α) was used to analyze surface element composition, valence states, and depth profiles. Work functions and valence band positions were determined by UPS (PHI5000 VersaProbe III). UV–Vis absorbance spectra were obtained using a Shimadzu UV-3600i Plus spectrometer. Steady-state PL measurements were carried

out with a Horiba FluoroMax-4 spectrofluorometer using a 150 W Xenon lamp at an excitation wavelength of 450 nm.

Photoelectrochemical measurements

All photoelectrochemical measurements were performed using a potentiostat (IviumStat.h, Ivium Technologies) under simulated AM 1.5 G illumination (100 mW cm^{-2}). A three-electrode setup was used, with the synthesized photoanode as the working electrode, Ag/AgCl (3 M KCl) as the reference electrode, Pt mesh as the counter electrode, and 1 M NaOH solution (Aladdin, 98.0%, dissolved in deionized water) as the electrolyte. The photoanode, with a 1×1 cm^2 exposed surface area, was vertically illuminated from the front. Potentials *versus* Ag/AgCl were converted to the reversible hydrogen electrode scale using the Nernst equation:

$$E_{RHE} = E_{Ag/AgCl} + 0.0592\,pH + E^o_{Ag/AgCl} \tag{2}$$

$E^o_{Ag/AgCl} = 0.1976$ at 25 °C. The *J–V* curves were recorded over a potential range of 0.6–1.8 V$_{RHE}$ at a scan rate of 20 mV s^{-1}, with no iR compensation required for this system. PEIS was conducted under 1 sun illumination across a frequency range of 100 kHz to 0.1 Hz. PEIS data were fitted to a two-RC-unit equivalent circuit model using Z-view software, with an inaccurate resistance value of 5%. Mott–Schottky plots were used to determine the flat band potential (E_{FB}) and charge carrier density by scanning from 0.1 to 1.5 V$_{RHE}$ at 1000 Hz without illumination. OCP transient decay was measured under the same conditions as the PEC measurements.

Data availability

The source data for Figs. 2–6 and Supplementary Figs. 2, 5–8, 10–13, 15–29, 31, 33–39 are provided as a Source Data file. Source data are provided with this paper.

References

1. Roger, I., Shipman, M. A. & Symes, M. D. Earth-abundant catalysts for electrochemical and photoelectrochemical water splitting. *Nat. Rev. Chem.* **1**, 0003 (2017).
2. Jeon, D. et al. Superaerophobic hydrogels for enhanced electrochemical and photoelectrochemical hydrogen production. *Sci. Adv.* **6**, eaaz3944 (2020).
3. Kim, J. H. et al. Toward practical solar hydrogen production - an artificial photosynthetic leaf-to-farm challenge. *Chem. Soc. Rev.* **48**, 1908–1971 (2019).
4. Liu, G. et al. Porous versus compact hematite nanorod photoanode for high-performance photoelectrochemical water oxidation. *ACS Sustain. Chem. Eng.* **7**, 11377–11385 (2019).
5. Rauf, A. et al. Tuning the optoelectronic properties of hematite with rhodium doping for photoelectrochemical water splitting using density functional theory approach. *Sci. Rep.* **11**, 41 (2021).
6. Li, C. C. et al. Surface, bulk, and interface: rational design of hematite architecture toward efficient photo-electrochemical water splitting. *Adv. Mater.* **30**, 1707502 (2018).
7. Mazzaro, R. et al. Hematite nanostructures: an old material for a new story. Simultaneous photoelectrochemical oxidation of benzylamine and hydrogen production through Ti doping. *Nano Energy* **61**, 36–46 (2019).
8. Kang, J. S. et al. Iron oxide photoelectrode with multidimensional architecture for highly efficient photoelectrochemical water splitting. *Angew. Chem. Int. Ed.* **56**, 6583–6588 (2017).
9. Wang, T. et al. Boosting hole transfer in the fluorine-doped hematite photoanode by depositing ultrathin amorphous FeOOH/CoOOH cocatalysts. *ACS Appl. Mater. Interfaces* **12**, 49705–49712 (2020).
10. Bai, J. W. et al. Reduction of charge carrier recombination by Ce gradient doping and surface polarization for solar water splitting. *Chem. Eng. J.* **448**, 137602 (2022).
11. Li, C. C. et al. Surviving high-temperature calcination: ZrO₂-induced hematite nanotubes for photoelectrochemical water oxidation. *Angew. Chem. Int. Ed.* **56**, 4150–4155 (2017).
12. Chai, H. et al. In₂S₃/F-Fe₂O₃ type-II heterojunction bonded by interfacial S–O for enhanced charge separation and transport in photoelectrochemical water oxidation. *Appl. Catal. B* **305**, 121011 (2022).
13. Hisatomi, T. et al. Enhancement in the performance of ultrathin hematite photoanode for water splitting by an oxide underlayer. *Adv. Mater.* **24**, 2699–2702 (2012).
14. Cao, D. P. et al. Cathodic shift of onset potential for water oxidation on a Ti⁴⁺ doped Fe₂O₃ photoanode by suppressing the back reaction. *Energy Environ. Sci.* **7**, 752–759 (2014).
15. Gonçalves, R. H. & Leite, E. R. The colloidal nanocrystal deposition process: an advanced method to prepare high performance hematite photoanodes for water splitting. *Energy Environ. Sci.* **7**, 2250–2254 (2014).
16. Yoon, K. Y. et al. NiFeOₓ decorated Ge-hematite/perovskite for an efficient water splitting system. *Nat. Commun.* **12**, 4309 (2021).
17. Yi, S. S. et al. Highly efficient photoelectrochemical water splitting: surface modification of cobalt-phosphate-loaded Co₃O₄/Fe₂O₃ *p–n* heterojunction nanorod arrays. *Adv. Funct. Mater.* **29**, 1801902 (2019).
18. Yi, S. S. et al. Coupling effects of indium oxide layer on hematite enabling efficient photoelectrochemical water splitting. *Appl. Catal., B* **283**, 119649 (2021).
19. Ahn, H. J. et al. MoSₓ supported hematite with enhanced photoelectrochemical performance. *J. Mater. Chem. A* **3**, 21444–21450 (2015).
20. Li, F. et al. Facile regrowth of Mg-Fe₂O₃/P-Fe₂O₃ homojunction photoelectrode for efficient solar water oxidation. *J. Mater. Chem. A* **6**, 13412–13418 (2018).
21. Xu, J. L. et al. Perovskite oxide LaNiO₃ nanoparticles for boosting H₂ evolution over commercial cds with visible light. *Chem. Eur. J.* **24**, 18512–18517 (2018).
22. Pareek, A. et al. Ultrathin MoS₂-MoO₃ nanosheets functionalized CdS photoanodes for effective charge transfer in photoelectrochemical (PEC) cells. *J. Mater. Chem. A* **5**, 1541–1547 (2017).
23. Huang, L. J. et al. Fabrication of hierarchical Co₃O₄@CdIn₂S₄ *p–n* heterojunction photocatalysts for improved CO₂ reduction with visible light. *J. Mater. Chem. A* **8**, 7177–7183 (2020).
24. Wang, C. L. et al. Activating a hematite nanorod photoanode *via* fluorine-doping and surface fluorination for enhanced oxygen evolution reaction. *Nanoscale* **12**, 3259–3266 (2020).
25. Zhang, H. M. et al. Gradient tantalum-doped hematite homojunction photoanode improves both photocurrents and turn-on voltage for solar water splitting. *Nat. Commun.* **11**, 4622 (2020).
26. Morales-Guio, C. G. et al. An optically transparent iron nickel oxide catalyst for solar water splitting. *J. Am. Chem. Soc.* **137**, 9927–9936 (2015).
27. Zhang, K. F. et al. Fe₂O₃/3DOM BiVO₄: high-performance photocatalysts for the visible light-driven degradation of 4-nitrophenol. *Appl. Catal. B* **202**, 569–579 (2017).
28. Kim, J. H. et al. Carbonate-coordinated cobalt co-catalyzed BiVO₄/WO₃ composite photoanode tailored for CO₂ reduction to fuels. *Nano Energy* **15**, 153–163 (2015).
29. Zhang, Y. F. et al. Enhanced visible-light photoelectrochemical performance via chemical vapor deposition of Fe₂O₃ on a WO₃ film to form a heterojunction. *Rare Met.* **39**, 841–849 (2020).
30. Kim, J. H. et al. Hetero-type dual photoanodes for unbiased solar water splitting with extended light harvesting. *Nat. Commun.* **7**, 13380 (2016).
31. Guo, F. et al. A generic concept to overcome bandgap limitations for designing highly efficient multi-junction photovoltaic cells. *Nat. Commun.* **6**, 7730 (2015).

32. Itoh, K. & Bockris, J. O. M. Stacked thin-film photoelectrode using iron oxide. *J. Appl. Phys.* **56**, 874–876 (1984).

33. Wang, S. C. et al. New BiVO₄ dual photoanodes with enriched oxygen vacancies for efficient solar-driven water splitting. *Adv. Mater.* **30**, 1800486 (2018).

34. Ummireddi, A. K. & Pala, R. G. S. Operating the stacked photoanode at the thickness of exciton diffusion length enhances the efficiency of photoelectrochemical water splitting. *J. Chem. Sci.* **133**, 37 (2021).

35. Nguyen, T. T. et al. Transparent stacked photoanodes with efficient light management for solar-driven photoelectrochemical cells. *ACS Appl. Mater. Interfaces* **13**, 10181–10190 (2021).

36. Niu, W. Z. et al. Extended light harvesting with dual Cu₂O-based photocathodes for high efficiency water splitting. *Adv. Energy Mater.* **8**, 1702323 (2018).

37. Zhang, Z. J. et al. Interfacial oxygen vacancies yielding long-lived holes in hematite mesocrystal-based photoanodes. *Nat. Commun.* **10**, 4832 (2019).

38. Zhang, H. M. & Lee, J. S. Hybrid microwave annealing synthesizes highly crystalline nanostructures for (photo)electrocatalytic water splitting. *Acc. Chem. Res.* **52**, 3132–3142 (2019).

39. Li, W. C. et al. Hole storage overlayer of amorphous hafnium oxide for boosting hematite-based solar water splitting. *Appl. Catal. B* **342**, 123465 (2024).

40. Qu, J. S. et al. Evolution of oxygen vacancies in cerium dioxide at atomic scale under CO₂ reduction. *Chem. Catal.* **3**, 100759 (2023).

41. Kment, S. et al. Photoanodes with fully controllable texture: the enhanced water splitting efficiency of thin hematite films exhibiting solely (110) crystal orientation. *ACS Nano* **9**, 7113–7123 (2015).

42. Wu, H. et al. Low-bias photoelectrochemical water splitting via mediating trap states and small polaron hopping. *Nat. Commun.* **13**, 6231 (2022).

43. Zhang, W. R. et al. Unconventional relation between charge transport and photocurrent via boosting small polaron hopping for photoelectrochemical water splitting. *ACS Energy Lett.* **3**, 2232–2239 (2018).

44. Pan, L. et al. Constructing TiO₂ p–n homojunction for photoelectrochemical and photocatalytic hydrogen generation. *Nano Energy* **28**, 296–303 (2016).

45. Wang, Y. C. et al. Formation of internal p–n junctions in Ta₃N₅ photoanodes for water splitting. *J. Mater. Chem. A* **2**, 20570–20577 (2014).

46. Guo, X. J. et al. Adsorption of antimony onto iron oxyhydroxides: adsorption behavior and surface structure. *J. Hazard. Mater.* **276**, 339–345 (2014).

47. Loiudice, A. et al. Bandgap tunability in Sb-alloyed BiVO₄ quaternary oxides as visible light absorbers for solar fuel applications. *Adv. Mater.* **27**, 6733–6740 (2015).

48. Annamalai, A. et al. Influence of Sb⁵⁺ as a double donor on hematite (Fe³⁺) photoanodes for surface-enhanced photoelectrochemical water oxidation. *ACS Appl. Mater. Interfaces* **10**, 16467–16473 (2018).

49. Kang, J. H. et al. Meso-pore generating P doping for efficient photoelectrochemical water splitting. *Nano Energy* **107**, 108090 (2023).

50. John, A. D. Lange's Handbook of Chemistry (McGraw-Hill, New York, 1998).

51. Kronawitter, C. X. et al. Titanium incorporation into hematite photoelectrodes: theoretical considerations and experimental observations. *Energy Environ. Sci.* **7**, 3100–3121 (2014).

52. Chen, Z., Dinh, H. & Miller, E. Photoelectrochemical water splitting: standards, experimental methods, and protocols (Springer, 2013).

53. Wilhelm, S. M. et al. Semiconductor properties of iron oxide electrodes. *J. Electrochem. Soc.* **126**, 419 (1979).

54. Zhang, J. F., Cui, J. Y. & Eslava, S. Oxygen Evolution catalysts at transition metal oxide photoanodes: their differing roles for solar water splitting. *Adv. Energy Mater.* **11**, 2003111 (2021).

55. Zhang, Y. C. et al. Rate-limiting O–O bond formation pathways for water oxidation on hematite photoanode. *J. Am. Chem. Soc.* **140**, 3264–3269 (2018).

56. Wang, S. C. et al. New iron-cobalt oxide catalysts promoting BiVO₄ films for photoelectrochemical water splitting. *Adv. Funct. Mater.* **28**, 1802685 (2018).

57. Zhang, B. H. et al. Novel Bi₂₊ₓWO₆ p–n homojunction nanostructure: preparation, characterization, and application for a self-powered cathodic photoelectrochemical immunosensor. *ACS Sens.* **5**, 2876–2884 (2020).

58. Wang, P. P. et al. Ultrathin cobalt oxide interlayer facilitated hole storage for sustained water oxidation over composited tantalum nitride photoanodes. *ACS Catal.* **11**, 12736–12744 (2021).

59. Nellist, M. R. et al. Potential-sensing electrochemical atomic force microscopy for in operando analysis of water-splitting catalysts and interfaces. *Nat. Energy* **3**, 46–52 (2018).

60. Laskowski, F. A. L. et al. Metal oxide/(oxy)hydroxide overlayers as hole collectors and oxygen-evolution catalysts on water-splitting photoanodes. *J. Am. Chem. Soc.* **141**, 1394–1405 (2019).

61. McCrory, C. C. L. et al. Benchmarking heterogeneous electrocatalysts for the oxygen evolution reaction. *J. Am. Chem. Soc.* **135**, 16977–16987 (2013).

62. Klahr, B. et al. Photoelectrochemical and impedance spectroscopic investigation of water oxidation with "Co–Pi"-coated hematite electrodes. *J. Am. Chem. Soc.* **134**, 16693–16700 (2012).

63. Iandolo, B. & Hellman, A. The role of surface states in the oxygen evolution reaction on hematite. *Angew. Chem. Int. Ed.* **53**, 13404–13408 (2014).

64. Le Formal, F. et al. Passivating surface states on water splitting hematite photoanodes with alumina overlayers. *Chem. Sci.* **2**, 737–743 (2011).

65. Zhong, M. et al. Surface modification of CoOₓ loaded BiVO₄ photoanodes with ultrathin p-type NiO layers for improved solar water oxidation. *J. Am. Chem. Soc.* **137**, 5053–5060 (2015).

66. Zaban, A., Greenshtein, M. & Bisquert, J. Determination of the electron lifetime in nanocrystalline dye solar cells by open-circuit voltage decay measurements. *ChemPhysChem* **4**, 859–864 (2003).

67. Wang, H. X. et al. Impact of NiCo₂O₄/SrTiO₃ p–n heterojunctions on the interface of photoelectrochemical water oxidation. *ACS Appl. Mater. Interfaces* **15**, 28739–28746 (2023).

68. Ros, C. et al. Degradation and regeneration mechanisms of NiO protective layers deposited by ALD on photoanodes. *J. Mater. Chem. A* **7**, 21892–21902 (2019).

69. Monllor-Satoca, D. et al. What do you do, titanium? Insight into the role of titanium oxide as a water oxidation promoter in hematite-based photoanodes. *Energy Environ. Sci.* **8**, 3242–3254 (2015).

70. Zhang, J. F. et al. Role of cobalt–iron (oxy)hydroxide (CoFeOₓ) as oxygen evolution catalyst on hematite photoanodes. *Energy Environ. Sci.* **11**, 2972–2984 (2018).

71. Lee, D. K. & Choi, K. S. Enhancing long-term photostability of BiVO₄ photoanodes for solar water splitting by tuning electrolyte composition. *Nat. Energy* **3**, 53–60 (2018).

72. Jian, J. et al. Embedding laser generated nanocrystals in BiVO₄ photoanode for efficient photoelectrochemical water splitting. *Nat. Commun.* **10**, 2609 (2019).

73. Zhang, Z. H., Hossain, M. F. & Takahashi, T. Self-assembled hematite (α-Fe₂O₃) nanotube arrays for photoelectrocatalytic degradation of azo dye under simulated solar light irradiation. *Appl. Catal. B* **95**, 423–429 (2010).

Acknowledgements

Author contributions

H.Z. and C.X. conceived the project. C.X. and H.W. fabricated the devices and performed the experiments. H.G., K.L., Y.Z., and W.L. assisted in the experiments. J.C., J.S.L., and H.Z. supervised the work and discussed the results. All authors contributed to the scientific discussion and manuscript revisions.

Competing interests

The authors declare no competing interests.

Additional information

Supplementary information The online version contains supplementary material available at https://doi.org/10.1038/s41467-024-53967-y.

Correspondence and requests for materials should be addressed to Junze Chen, Jae Sung Lee or Hemin Zhang.

Peer review information *Nature Communications* thanks Sixto Gimenez, Jinlu He, Thomas Wågberg and Giovanni Zangari for their contribution to the peer review of this work. A peer review file is available.

Reprints and permissions information is available at http://www.nature.com/reprints

Publisher's note Springer Nature remains neutral with regard to jurisdictional claims in published maps and institutional affiliations.